Investigation of oxide crystals by means of synchrotron and conventional X-ray diffraction topography

Wojciech Wierzchowski[1], Agnieszka Malinowska[1], Krzysztof Wieteska[2], Edyta Wierzbicka[1], Krystyna Mazur[1], Maria Lefeld - Sosnowska[3], Marek Świrkowicz[1], Tadeusz Łukasiewicz[1]

X-ray diffraction topography, exploring both conventional and synchrotron sources of X-rays, has been widely used for the investigation of the structural defects in crystals of oxides. The majority of bulk oxide crystals have been grown by the Czochralski method from a melted mixture of high purity oxides. Some important oxide crystals like quartz and ZnO have been obtained by the hydrothermal method. In the case of crystals grown by the first method, synchrotron diffraction topography can be and was used for studying individual dislocations and their complexes (e.g. glide bands, sub-grain boundaries), individual blocks, twinning, the domain structure and various segregation effects negatively affecting crystal properties. What is more, the topographical investigation can provide information concerning the reasons for the generation of the defects, which becomes useful for improving the growth technology. In the present paper the possibilities of the diffraction topography are discussed on the basis of several investigations of the oxide crystals, in particular garnets, orthovanadates, mixed calcium barium and strontium niobates as well as praseodymium lanthanum aluminates. The majority of the results refer to oxide crystals grown at the Institute of Electronic Materials Technology (ITME). The synchrotron investigations included in the paper were performed by the authors at the HASYLAB Synchrotron Laboratory in Hamburg.

Key words: X-ray diffraction topography, crystal lattice defects, Czochralski method

Badanie monokryształów tlenkowych za pomocą synchrotronowej i konwencjonalnej rentgenowskiej topografii dyfrakcyjnej

Rentgenowska topografia dyfrakcyjna, wykorzystująca zarówno konwencjonalne, jak i synchrotronowe źródła promieniowania rentgenowskiego, jest od wielu lat z powodzeniem stosowana do badania defektów strukturalnych w różnego rodzaju monokryształach. Szeroką grupę tych materiałów stanowią kryształy tlenkowe, które w większości są otrzymywane metodą Czochralskiego ze stopionej mieszaniny tlenków o wysokiej czystości. Do otrzymywania kryształów tlenków, takich jak kwarc i ZnO, stosuje się metodę hydrotermalną. Rentgenowska topografia dyfrakcyjna może być wykorzystana do badania indywidualnych dyslokacji i ich kompleksów (np. pasma poślizgowe, granice niskokątowe), pojedynczych bloków, zbliźniaczeń, struktury domenowej i różnych efektów segregacyjnych. Wszystkie te defekty mogą wpływać negatywnie na jednorodność i właściwości kryształów. Badania topograficzne mogą również dostarczyć informacji dotyczących przyczyn powstawania defektów, co przydatne jest w doskonaleniu technologii. W niniejszej pracy omówiono możliwości topografii dyfrakcyjnej na podstawie przeprowadzonych badań szeregu kryształów tlenkowych, w szczególności granatów, ortowanadianów, mieszanych niobianów wapnia, baru i strontu oraz glinianów prazeodymu i lantanu. Większość wyników dotyczy monokryształów tlenków otrzymywanych w Instytucie Technologii Materiałów Elektronicznych (ITME). Uwzględnione badania synchrotronowe zostały przeprowadzone przez autorów w Laboratoriom Synchrotronowym HASYLAB w Hamburgu.

Słowa kluczowe: dyfrakcyjna topografia rentgenowska, defekty sieci krystalicznej, metoda Czochralskiego

1. Introduction

The important group of crystals, which is widely used for several applications, particularly in the laser technology and in the technology of electronic devices are oxide crystals, built either from single oxides or a mixture of oxides [1 - 11]. These crystals provide an important field for the application of X-ray diffraction topography exploring both conventional and synchrotron radiation sources.

The majority of oxide crystals are not soluble in water in normal conditions and they are useful for the preparation of durable elements, convenient for most of the applications. The majority of the bulk oxide crystals are therefore grown by the Czochralski method from a melted mixture of high purity oxides. Only some of them are obtained by means of the floating zone method (recently also with optical heating) [5 - 6]. Some important oxide crystals like quartz and ZnO [7 - 11] are grown by the hydrothermal method. In the last case the crystal grow

from an aqueous solution, formed under high pressure at high temperatures. The crystals obtained by means of the hydrothermal method are to some extend analogous to those obtained from an aqueous solution, containing various growth sectors corresponding to some low indexed crystallographic planes. The differences in growth rates and segregation parameters for the various growth planes result in differences of lattice parameters and segregation effects, usually causing the strains in the growth sector boundaries. The Bridgman, flux and Verneuils methods have also been sometimes used [12].

X-ray diffraction topography [12 - 24] is a method, which can be effectively used for the characterization of oxide crystals. It includes in fact a number of methods differing in the experimental arrangement and consequently in the mechanism of contrast formation and in the sensitivity. The general principle of the methods consists in recording contrast inhomogeneities in the diffracted beam due to long range strain fields related to lattice defects/crystal deformations with a very high spatial resolution. The forward diffracted one could also be used, but it happens rather rarely.

X-ray diffraction topographic methods enable the identification of the defects, especially dislocations, stacking faults and regularly shaped inclusions. The identification of the defects in X-ray diffraction topography includes the analysis of contrast extinction in various crystallographically equivalent reflections and simulation of the topographic contrasts [12 - 14]. The topographic methods are usually more effective with the synchrotron radiation than with the conventional radiation thanks to the possibility of better resolution, a better collimation and an access to more suitable wavelength forming the image [25 - 30]. The numerical simulation of diffraction contrast [12 - 14] can presently be used practically in the case of all topographic methods.

A significant new step in the development of the laboratory based diffraction topography was the recent introduction of a new Micron XRT apparatus from Rigaku [26 - 27]. The equipment uses a fine focus rotating generator and a special parabolic mirror forms a nearly parallel beam. High intensity of the beam enables the use of a CCD camera with resolution close to 2 μm.

Conventional topographic investigations of the Czochralski-grown oxide crystals have been published in [33 - 41], while the crystal grown by the hydrothermal method in [45 - 54]. Synchrotron topographic investigations of oxide crystals have been published in [36 - 46, 63], in particular by Baruchel et al. [45], Kasper et al. [46], Yao et al. [47], Muehlberg et al. [48], Prokhorov et al. [49], Yoneda et al. [50] and by Dudley and Yao [51 - 52] and Malinowska et al. [55]. An interesting synchrotron topographic method is so called *stroboscopic topography* [53 - 54]. It can be carried out in the piezoelectric crystals, particularly lithium niobates and it reveals the strain which appears in the course of the induced oscillations.

The present paper will illustrate the possibilities of the conventional and synchrotron X-ray topography for the Czochralski-grown crystals as well as some more detailed experimental problems being the result of the investigations performed by the authors, and published elsewhere [55 - 72]. These results include synchrotron topographic investigations performed at HASYLAB, the details of which are described in [57].

2. Growth of oxide crystals

The most popular method of growing the oxide crystal is the Czochralski method, in which the crystals are grown from the suitably composed mixture of melted oxides. However, recently the floating-zone method including optical heating furnaces instead of the inductive coils [5 - 6] has also been applied. The equipment used for the growth of single crystals from melted oxides by the Czochralski method is shown in Fig. 1a, while the schema of the floating-zone
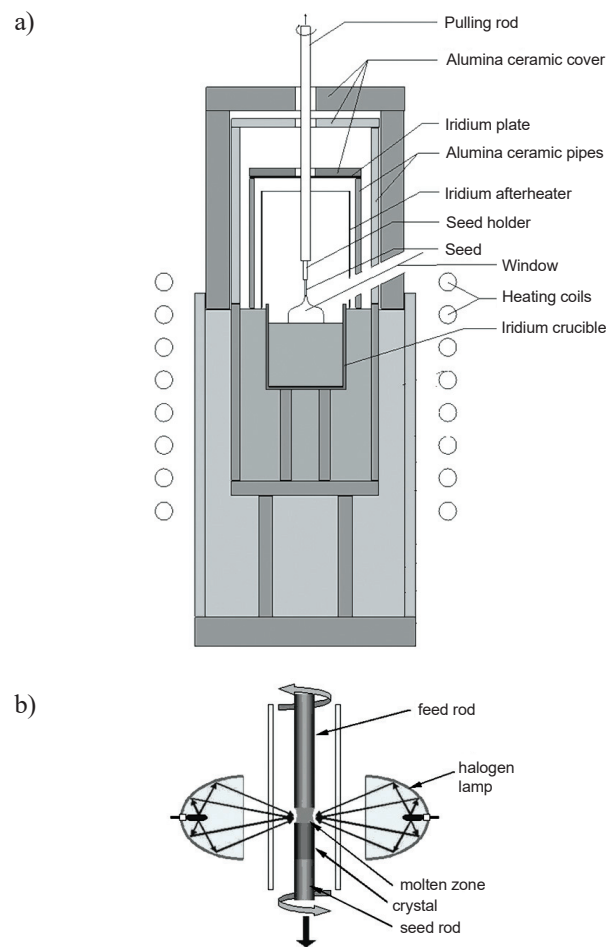

Fig. 1. Most frequently used methods of oxide crystals growth: (a) the Czochralski method, (b) the optical floating zone method [5, 81].
Rys. 1. Najczęściej stosowane metody wzrostu kryształów tlenkowych: (a) metoda Czochralskiego, (b) metoda topienia strefowego [5, 81].

method with optical heating is shown in Fig. 1b. In the hydrothermal method the crystals are grown from aqueous solutions obtained at high temperatures and under very high pressure. The last method was used in specific cases, e.g. for growing quartz and zinc oxide crystals.

Experimental results included in the present paper have been obtained with crystals grown by the Czochralski method and by the hydrothermal method in the Institute of Electronic Materials Technology. In the first case the oxide crystals were grown in an inductively heated iridium or platinum crucible and with a passive after heater. Starting materials with 4N purity were heated at the temperatures up to 1000°C for 6 hours before weighing, mixing and melting. The initial composition should compensate the effects of eventual evaporation. Single crystals with 20 mm diameter were grown on iridium 2 mm rod

with the pulling rate of 3 - 4 mm/h and the rotation of 4 - 6 rpm. Crystals were grown under ambient pressure in a nitrogen atmosphere, but sometimes the growing atmosphere contained an admixture of oxygen.

3. X-ray diffraction topography

The X-ray conventional topography of oxide crystals is usually carried out by means of two most popular methods. The most effective single crystal method (shown schematically in Fig. 2a) has been proposed by Lang [15 - 16], while the double-crystal topographic method (Fig. 2b) has been proposed by Bond and Andrus [17] but
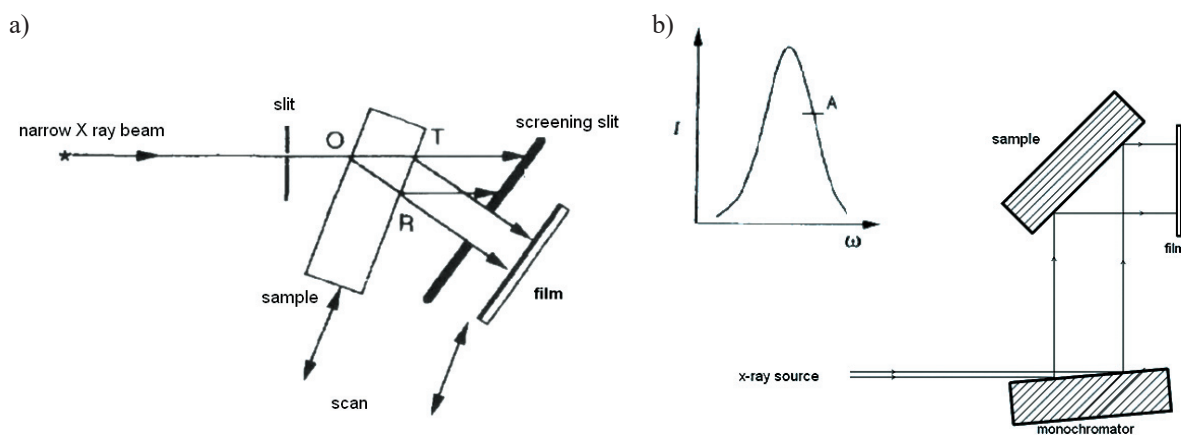

Fig. 2. Schema of the two most important topographic methods of the conventional X-ray diffraction topography: (a) the Lang projection (and section) topography [15 - 16], and (b) the double crystal topography – the schema of the arrangement, with significantly asymmetric reflection at the monochromator proposed by Renninger [20].

Rys. 2. Schematy dwóch najważniejszych metod konwencjonalnej rentgenowskiej topografii dyfrakcyjnej: (a) projekcyjna (i przekrojowa) topografia Langa [15 - 16], i (b) topografia dwukrystaliczna – schemat układu z asymetrycznym odbiciem na monochromatorze zaproponowany przez Renningera [20].
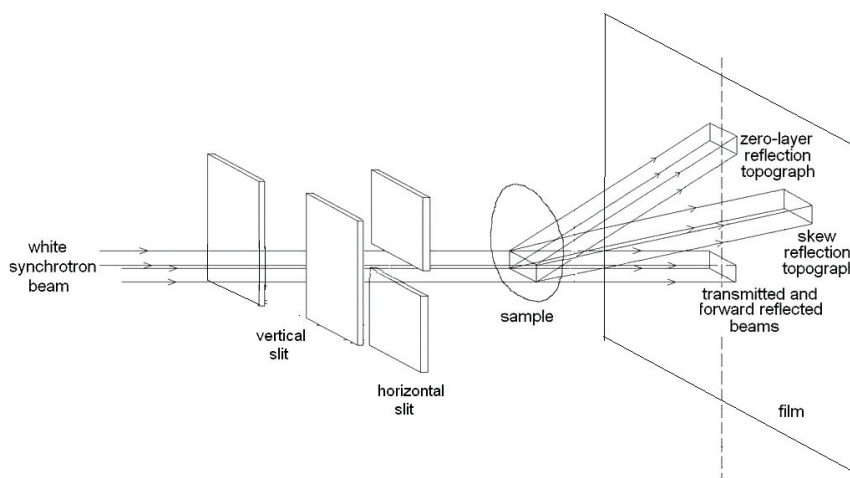

Fig. 3. The scheme of the synchrotron white beam topography in transmission case [57].

Rys. 3. Schemat synchrotronowej topografii w wiązce białej dla przypadku transmisyjnego [57].
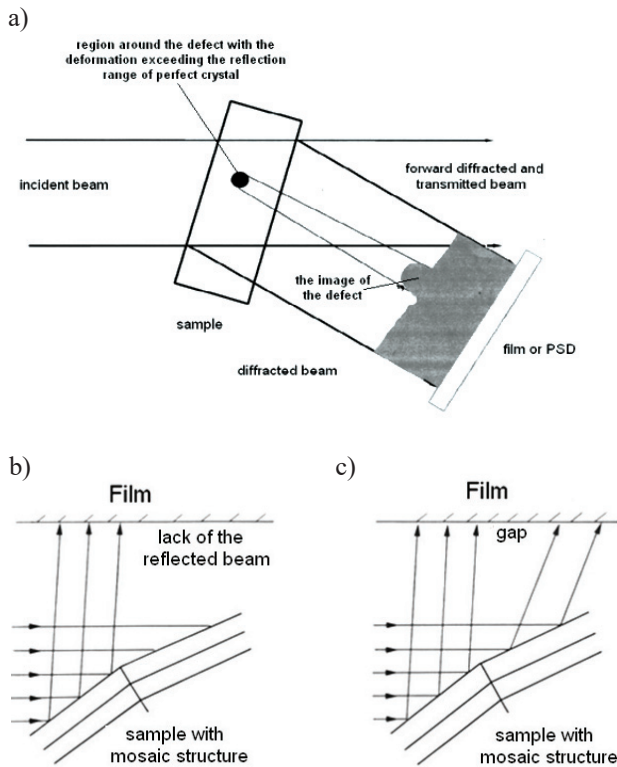
a)

b)   c)

Fig. 4. Schema of contrast formation in the X-ray diffraction topography: (a) – reproduction of isolated defects surrounded by almost perfect crystal (transmission case), (b), (c) formation of contrast from differently oriented parts of the crystals, respectively in the monochromatic and white beam of X-rays. According to [12 - 14, 78].

Rys. 4. Schemat powstawania kontrastu w rentgenowskiej topografii dyfrakcyjnej: (a) – przypadek transmisyjny dla pojedynczego defektu w krysztale prawie idealnym, (b), (c) tworzenie kontrastu dla różnie zorientowanych części kryształu, odpowiednio dla wiązki monochromatycznej (b) i białej (c) promieniowania X. Na podstawie [12 - 14, 78].

effectively used for revealing the dislocations by Bonse and Keppler [18]. The further extensions of the double-crystal method were described in [19 - 21]. The earlier topographic methods were revealed by Shultz [17], Berg [18] and Barrett [19].

Bending magnets were the sources of the synchrotron radiation in the case of presently described topographic experiments at DORIS III. They allowed obtaining the photon energy in the range from 5 to 35 keV. The energy was satisfactory for most of the topographic investigation. The present investigations of the oxide crystals were carried out at the two experimental stations at HASYLAB, the white beam station F1 and the monochromatic beam station E2 [57].

A schema of the arrangement for synchrotron white beam topography is shown in Fig. 3. The beam limited by a system of vertical and horizontal slits is entering the crystals providing a kind of Laue pattern either in the Laue-case (transmission) or Bragg-case (reflection). Thanks to small apparent diameters of the synchrotron source,

of approximately 0.5 mm in vertical direction and 2 mm wide and large 18 m distance of the experimental station from the bending magnet, each Laue spot is a high resolution topograph revealing the defects in the investigated crystal. At the typical distances of film to crystal of 15 cm the geometrical resolution is better than 5 μm. The synchrotron topographic investigations were usually performed both in the back-reflection and in the transmission case, exposing the projection and section topographs. In the case of the section topography it was possible to reduce the width of the slit to 5 μm.

Most often the so called *extinction contrast* is formed in a single crystal white beam projection topography in the Bragg - case and in the Laue - case at small absorption. The defects are revealed thanks to the additional intensity contributed by a region of defect *outside the reflection range* fulfilling the condition [24, 54]:

$$|4\sin \Theta \frac{\partial \vec{u}(\vec{r}) \cdot \vec{h}}{\partial s_h}| > \delta. \qquad (1)$$

Here $\vec{u}(\vec{r})$ is the displacement vector connected with the defect, $\vec{h}$ is the diffraction vector and s_h is the coordinate along the reflected beam. This condition indicates that wider images of dislocations can be obtained when the width of the reflection range is small. The very important parameter, characterizing the possibilities of revealing the defects is the range of reflection predicted by the dynamical theory [9]:

$$\delta = \frac{2|C|}{\sin (2\vartheta_b)} \sqrt{\frac{\gamma_0}{|\gamma_h|} \chi_h \chi_{\bar{h}}}. \qquad (2)$$

The polarization factor $C = |\cos 2\Theta|$ for the π-polarization in the plane of diffraction and $C = 1$ for σ-polarization perpendicular to the plane of diffraction, $\chi_{h,0}$ are the coefficient of the Fourier expansion of dielectric susceptibility, proportional to the structural factors.

The anomalous transmission contrast (also called dynamical contrast) is observed when attenuation is strong – and the defects become revealed thanks to the destruction of the *anomalous transmission*. The last effect consists in fitting the excited wave-field to the reflecting planes causing a significant decrease of absorption. Due to the anomalous transmission it is otherwise possible to obtain the transmission topographs in highly absorbing crystals built of the element with large atomic number, as the anomalous absorption can be even of two orders lower than the normal photoelectrical absorption. In addition the synchrotron sources offer another great help in studying such crystals, as they give the possibility to use reflections fulfilling the Bragg condition for very short wavelength and thus with low absorption.

A different contrast mechanism is present in the case of the double-crystal topography, which may be interpreted as the result of local shifts of the rocking curve

angular position (with respect to a reference area) caused by the strain field (for example dislocations) or chemical compositions changes (segregation effects). The observed change of the reflected intensity ΔI may be written [17]:

$$\Delta I = \frac{dP(\Theta)}{d\Theta}\left[\frac{\Delta d}{d}\,\mathrm{tg}\Theta + \Delta\Theta_g\right]. \qquad (3)$$

The first term describes the change of the Bragg angle and the second the misorientation component in the plane of diffraction. The derivative of rocking curve $P(\Theta)$ is taken at the angular setting where the topograph is exposed. This means that the contrast strongly depends on the angular setting. It is the strongest on the steep slopes of the rocking curve and inverts coming to the opposite slope. In some cases the topographs taken at the slope allow to reveal the relative lattice parameter changes $\Delta a/a$ on the level 10^{-8}.

An oxide crystal can have different chemical composition, which influence the width of reflection and the contrast of the defect images. In general the X-ray diffraction topography provides weaker contrast on dislocations and other defects in the case of the crystals built of the atoms with larger atomic number.

The images of individual defects are often accompanied by some interference effects often caused by the decomposition of wave-fields. Obtaining the theoretical simulated images reproducing such fringes is possible with the use of numerical integration of the Takagi-Taupin equations [14].

The white beam synchrotron topography is more strictly equivalent to the Shultz [22] method than to the conventional Lang method, especially in the case when the crystal contains several disoriented parts. The white-beam topographic images of almost perfect crystals containing individual defects are, however, very similar to those obtained using the Lang method. The most important element of the setup used for synchrotron monochromatic beam topography was the monochromator equipped with two silicon crystals using respectively 333 and 511 reflections, but in many aspects the method is similar to the conventional double crystal topography.

In the case of highly deformed, e.g. elastically bent samples, the double-crystal topography and synchrotron monochromatic beam topography are often highly restricted to a narrow stripe. In such situations the so called *zebra pattern* technique [21] is very helpful, where a series of exposures with step-wise altered angular position is recorded on the same film.

4. Discussion of the representative results

The first representative examples of the use of X-ray diffraction topography refer to the crystals newly developed at ITME. Figs. 5 and 6 present the representative X-ray diffraction topographs of the $MgAl_2O_4$ samples obtained using the Lang and double crystal method including the zebra pattern technique [79]. The crystal in Fig. 5 contained the core formed of several facets and a number of volume defects – most of them are solute trails around the core and close to the crystal boundaries. The representative X-ray diffraction topographs
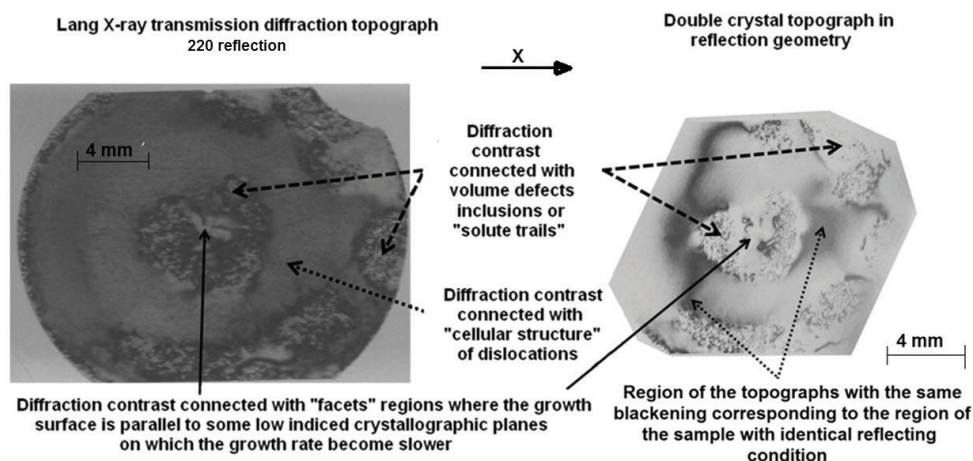

Fig. 5. The representative X-ray diffraction topographs obtained respectively using the Lang transmission method (220 reflection, $MoK\alpha_1$) and the double crystal method (533 reflection, $CuK\alpha_1$) the sample cut out from the $MgAl_2O_4$ crystal with 0.135 at. % of cobalt. The crystal contains the rod formed of several facets and a number of volume defects around the rod and close to the crystal boundaries – most of them are the solute trails. According to [79].

Rys. 5. Wybrane rentgenowskie topogramy dyfrakcyjne próbki $MgAl_2O_4$ 0,135 % at. Co wykonane metodą transmisyjnej topografii Langa (refleks 220, $MoK\alpha_1$) oraz metodą topografii dwukrystalicznej (refleks 533, $CuK\alpha_1$). Kryształ zawiera rdzeń utworzony przez obszary ściankowane oraz dużą ilość defektów objętościowych wokół rdzenia i blisko brzegu kryształu – wiele z nich to defekty typu *solute trials*. Na podstawie [79].
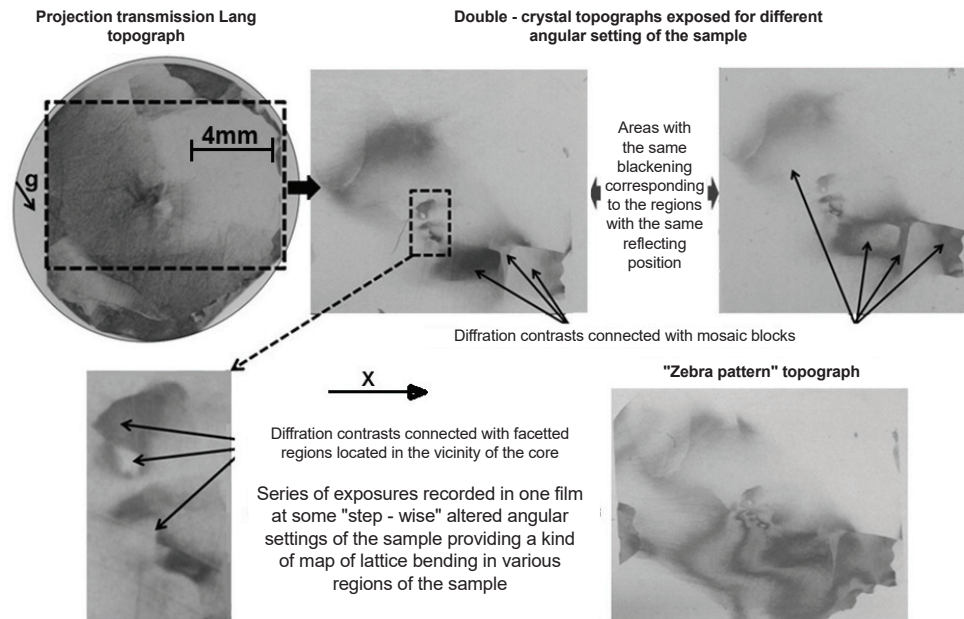
Projection transmission Lang topograph

Double - crystal topographs exposed for different angular setting of the sample

4mm

g

Areas with the same blackening corresponding to the regions with the same reflecting position

Diffration contrasts connected with mosaic blocks

X

Diffration contrasts connected with facetted regions located in the vicinity of the core

Series of exposures recorded in one film at some "step - wise" altered angular settings of the sample providing a kind of map of lattice bending in various regions of the sample

"Zebra pattern" topograph

Fig. 6. The representative X-ray diffraction topographs obtained using the Lang transmission method in 220 reflection (MoKα_1 radiation) and the double crystal method (including the zebra pattern technique) in 533 reflection (CuKα_1 radiation) of another sample cut out from the MgAl$_2$O$_4$ crystal with 0.286 at. % of cobalt. The crystal contains a similar rod as in Fig. 5 and a number of volume defects as solute trails around the rod and close to the crystal boundaries. Additionally some slightly disoriented grains are revealed. According to [79].
Rys. 6. Wybrane rentgenowskie topogramy dyfrakcyjne próbki MgAl$_2$O$_4$ 0,286 % at. Co wykonane metodą transmisyjnej topografii Langa (refleks 220, promieniowanie MoKα_1) oraz metodą topografii dwukrystalicznej (łącznie z techniką typu *zebra pattern*) (refleks 533, promieniowanie CuKα_1). Kryształ zawiera podobny rdzeń jak w przypadku próbki z Rys. 5. oraz dużą ilość defektów objętościowych typu *solute trials* otaczających obszar rdzenia oraz występujących blisko brzegu kryształu. Na podstawie [79].
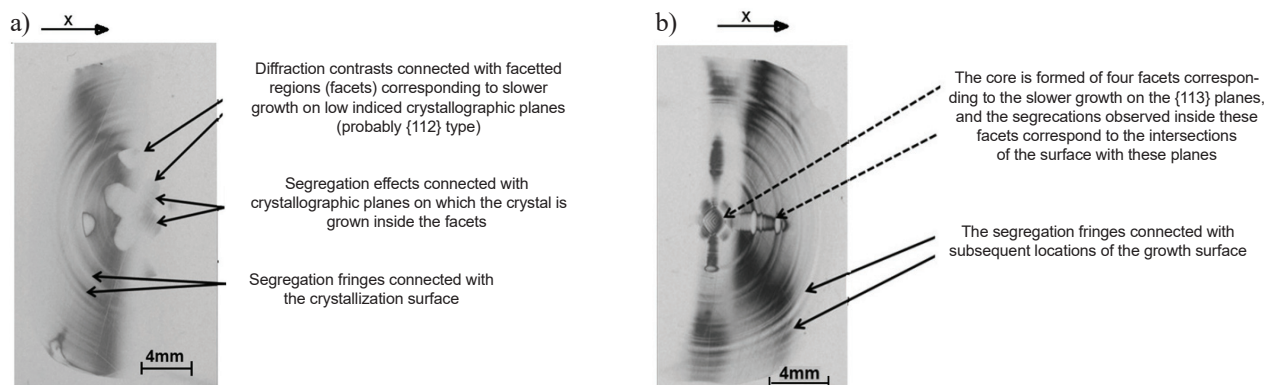

a) X

Diffraction contrasts connected with facetted regions (facets) corresponding to slower growth on low indiced crystallographic planes (probably {112} type)

Segregation effects connected with crystallographic planes on which the crystal is grown inside the facets

Segregation fringes connected with the crystallization surface

4mm

b) X

The core is formed of four facets corresponding to the slower growth on the {113} planes, and the segregations observed inside these facets correspond to the intersections of the surface with these planes

The segregation fringes connected with subsequent locations of the growth surface

4mm

Fig. 7. Conventional double crystal topographs in 840 reflection in CuKα_1 of the samples cut out from two LuYAG crystals, doped with 0.2 at.% (a) and 0.16 at.% (b) of praseodymium, revealing segregation fringes and some sets of facetted regions corresponding to various low indexed crystallographic planes, where the growth rate becomes slower. According to [80].
Rys. 7. Konwencjonalne topogramy dwukrystaliczne (refleks 840, promieniowanie CuKα_1) próbki LuYAG domieszkowanej 0,2% at. Pr (a) i 0,16% at. Pr (b). Topogramy ujawniają prążki segregacyjne oraz pewne układy obszarów ściankowanych odpowiadających wolniejszemu wzrostowi na płaszczyznach krystalograficznych o niskich wskaźnikach. Na podstawie [80].

of another sample are presented in Fig. 6. It was cut out from the MgAl$_2$O$_4$ crystal containing the similar rod. In this case there was a number of volume defects trails around the rod and close to the crystal boundaries, but additionally some slightly disoriented grains were also visible.

In Fig. 7 we report some representative double crystal topographs of (Lu$_{0.75}$Y$_{0.25}$)$_3$Al$_5$O$_{12}$ (LuYAG-75) crystals [80], which are new materials developed for modern scintillator crystals intended to be used for positron gene-

ration tomography, as well as for some spaceship probes. In this case, a very high attenuation of the molybdenum and copper radiation by yttrium, lutetium, and praseodymium admixture significantly disturb the possibility of making the conventional transmission topographs, but the defects may be successfully revealed by the double crystal topographic method.

The presently developed technology enabled obtaining very efficient (Lu$_{0.75}$Y$_{0.25}$)$_3$Al$_5$O$_{12}$ (LuYAG-75) and Lu$_3$Al$_5$O$_{12}$ (LuAG) scintillators. As it may be seen in Fig. 7,

the characteristic defects in these crystals are the distinct segregation fringes and various facets – the regions where the crystallization surface become parallel to some low indexed crystallographic planes, on which the growth rate become slower [80]. The last phenomenon is responsible for the characteristic appearance of the crystals grown from solutions, but also from vapour and the melt.

The formation of the facets was effectively followed by the complementary use of the projection synchrotron topography and synchrotron section topography, which allowed fitting the regions of facets and actual inclination of the growth surface in the case of $Yb_3Al_5O_{12}$ (YbYAG) crystals [66]. The topographs presenting a typical set of facets for two differently shaped growth surfaces are shown in Fig. 8.

The observed facets formed characteristic patterns, differing in different samples. It is well known that the most probable reason of facet formation is the coincidence of the orientation of growth surfaces with low indexed crystallographic planes. The growth velocity is usually slower in the direction perpendicular to these planes leading to slower growth in facetted regions and the constitutional supercooling. The facets may be identified as corresponding to {221}, {211}, {311} and {301} planes as it is shown schematically in Fig. 9. The first three {221} facets usually form a core, observed in most of the crystals, sometimes neighbouring with {211} ones. The third type of facets corresponds to the planes inclined at 43° and it occurs mostly for convex growth surface. The identification of the facets was confirmed by the transmission section topographs shown in Fig. 10, that allowed the observation of the location of the growth bands in the intersection of the sample with the incident synchrotron beam. It should also be noted that the topograph in Fig. 10b
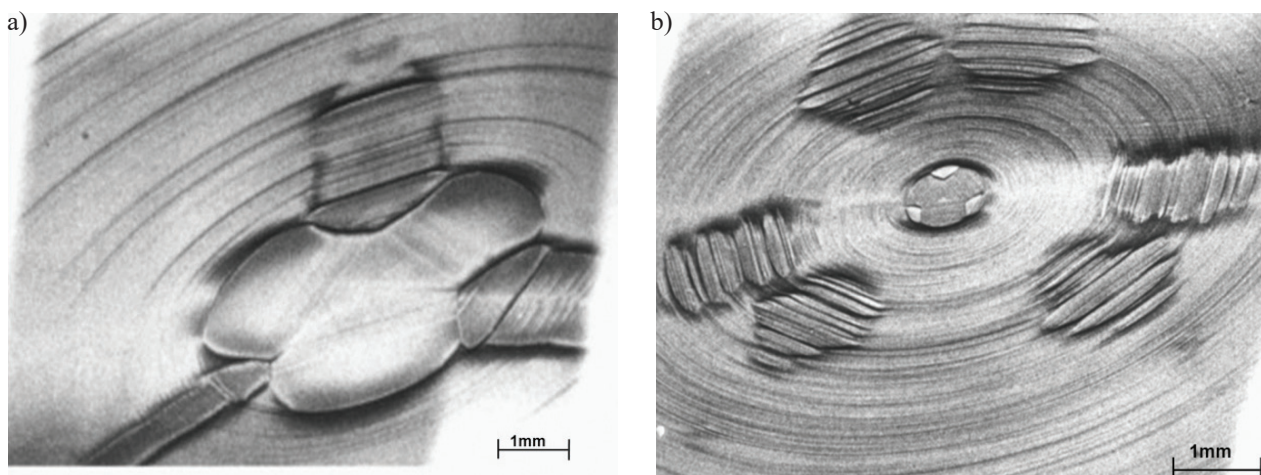
Fig. 8. White beam projection reflection topographs of Er-doped $Yb_3Al_5O_{12}$ crystals revealing segregation fringes and sets of facets; doping level: (a) 10 at. % Er and (b) 1.5 at. % Er; (a) 422 reflection, 0.0872 nm radiation, (b) 112 reflection, 0.4 nm radiation. According to K. Kołodziejak et al. [66].

Rys. 8. Odbiciowe topogramy projekcyjne w wiązce białej monokryształów $Yb_3Al_5O_{12}$ domieszkowanych erbem (10 % at. (a) i 1,5 % at. (b)) ujawniające prążki segregacyjne i układy obszarów ściankowanych; (a) refleks 422, promieniowanie 0,0872 nm, (b) refleks 112, promieniowanie 0,4 nm. Na podstawie K. Kołodziejak i in. [66].
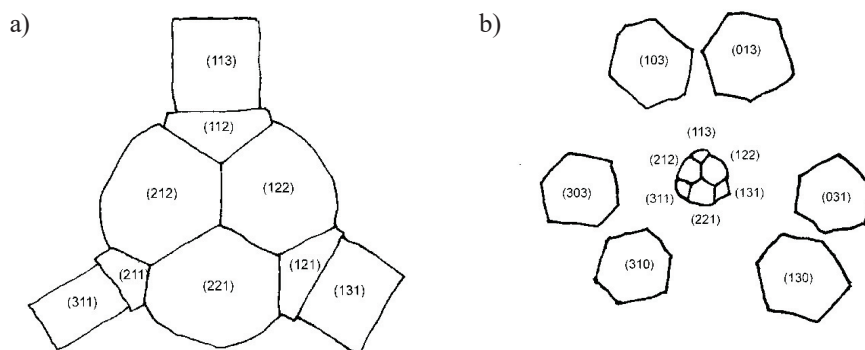
Fig. 9. (a), (b)The schema of identified facets corresponding respectively to the topographs in Fig. 8a, and b. According to K. Kołodziejak et al. [66].

Rys. 9. Schematy układu ścianek z przypisanymi wskaźnikami odpowiadające topogramom z Rys. 8a i 8b. Na podstawie K. Kołodziejak i in. [66].
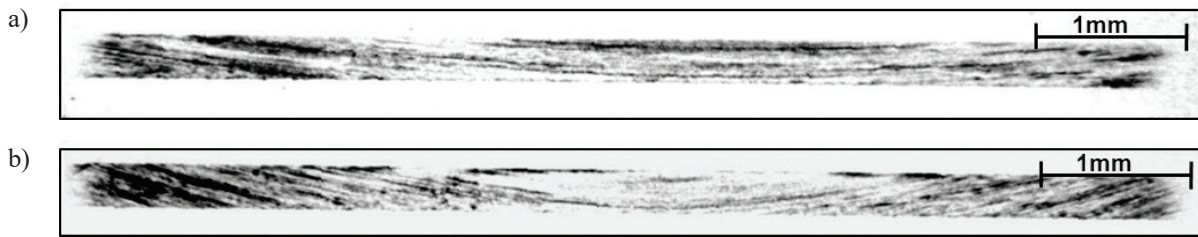
a)

b)

Fig. 10. Transmission white-beam section topographs of Er-doped $Yb_3Al_5O_{12}$ samples taken in $(\bar{1}6\bar{1}\bar{1})$ reflection, of 0.052 nm radiation and revealing the striation fringes corresponding to the successive location of growth surfaces in the plane intersected by the narrow incident beam perpendicular to the sample. Doping level: (a) 30 at. % and (b) 1.5 at. %. Thickness of both samples is 550 μm, the horizontal edge of the topographs is 8 mm. According to K. Kołodziejak et al. [66].

Rys. 10. Transmisyjne przekrojowe topogramy w wiązce białej monokryształów $Yb_3Al_5O_{12}$ domieszkowanych erbem (30% at. (a) i 1,5% at. (b)); refleks $(\bar{1}6\bar{1}\bar{1})$, promieniowanie 0,052 nm. Topogramy ujawniają prążki segregacyjne odpowiadające kolejnym położeniom powierzchni wzrostu w płaszczyźnie przecięcia kryształu wąską wiązką padającą prostopadle do próbki. Grubość próbek 550 μm, szerokość poziomej krawędzi topogramu – 8 mm. Według K. Kołodziejak i in. [66].
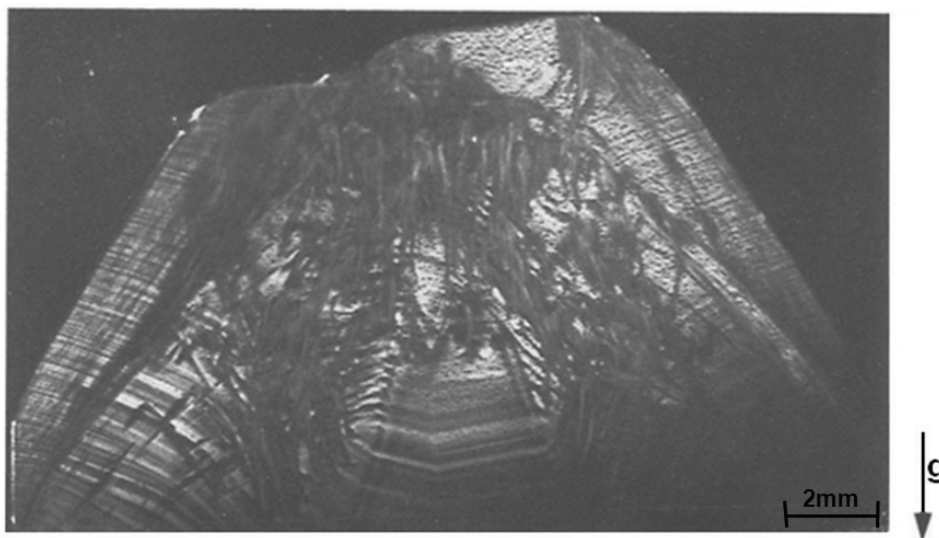

Fig. 11. Representative Lang topograph (direct copy) of the sample cut out along the growth axis from the initial part of the YAG crystal; 440 reflection, CuKα_1 radiation. According to K. Mazur and W. Wierzchowski [56].

Rys. 11. Wybrany topogram Langa (kopia bezpośrednia) próbki wyciętej równolegle do osi wzrostu z części początkowej kryształu YAG; refleks 440, promieniowanie CuKα_1. Według K. Mazur i W. Wierzchowski [56].
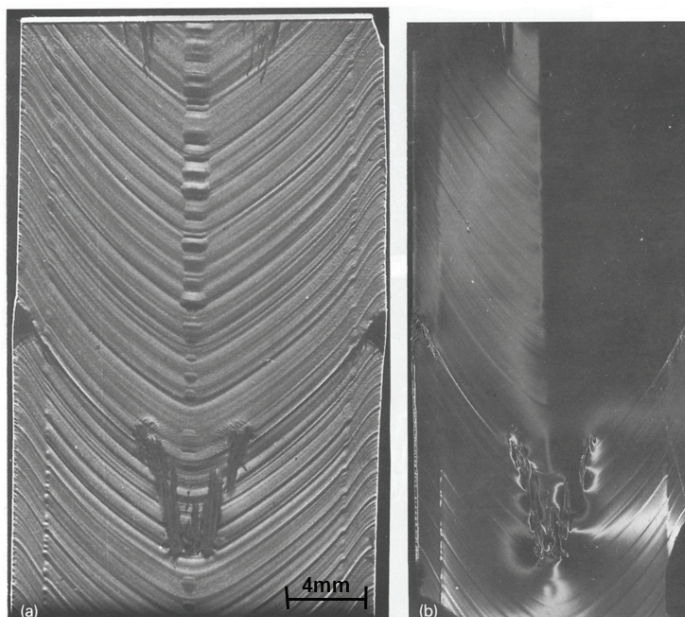

Fig. 12. (a) Lang topograph of the sample cut along the [111] growth axis from the middle part of Nd doped YAG crystal; 422 reflection, CuKα_1 radiation. The diffraction vector is located horizontally; (b) the double crystal topograph of the thicker sample cut close to that shown in (a); exposition in 620_{Si}-888_{YAG} arrangement, direct copies. According to K. Mazur and W. Wierzchowski [56].

Rys. 12. (a) Topogram Langa próbki wyciętej równolegle do osi wzrostu [111] ze środkowej części kryształu YAG:Nd; refleks 422, promieniowanie CuKα_1. Kierunek wektora dyfrakcji w poziomie; (b) topogram dwukrystaliczny grubszej próbki wyciętej w pobliżu próbki (a); ekspozycja w układzie 620_{Si}-888_{YAG}, kopia bezpośrednia. Na podstawie K. Mazur i W. Wierzchowski [56].
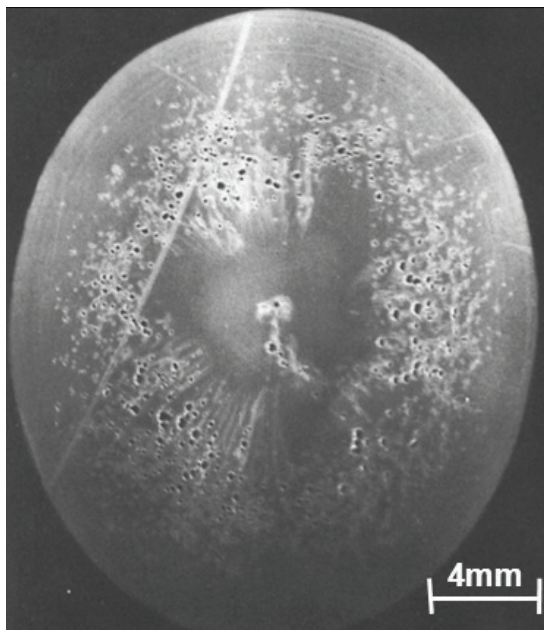
Fig. 13. Berg-Barrett topograph of the YAG sample exhibiting *reflecting* and *not-reflecting* volume defects, corresponding to *solute trails*; 751 reflection, CuKα_1 radiation, direct copy. According to K. Mazur and W. Wierzchowski [56].

Rys. 13. Topogram Berga-Barretta próbki YAG ujawniający *odbijające* i *nieodbijające* defekty objętościowe odpowiadające s*olute trails*; refleks 751, promieniowanie CuKα_1, kopia bezpośrednia. Według K. Mazur i W. Wierzchowski [56].

reveals some black dot-like contrasts, which may correspond to dislocations [66].

The representative transmission topograph of the samples cut out from the initial parts of the $Y_3Al_5O_{12}$ (YAG) crystals is shown in Fig. 11 [56]. We may notice that in the majority of crystals the growth surface is parabolic. At the very first stages of the growth, the surface is relatively flat and the core is not present. It starts to appear when the growth surface becomes more concave. Inside facets the growth bands are inclined at approximately 20° to the (111) plane. That is consistent with the arrangement of facets seen in the topographs of the samples perpendicular to the growth axis and points that the facets correspond to {112} planes. The topographs exhibit sequences of growth bands, corresponding to the growth conditions changes. Following the equivalent parts of growth bands with an analogous pattern from the core inside and in the rest of the crystal it may be found that the core grew a little deeper in the melt, probably in the zone where the stream of convection is pointing down to the melt. In many cases also the change of the growth bands curvature is observed at the distance approximately 1/3 of the crystal radius from the crystal boundaries. This curvature change also corresponds most probably to the zones with different directions of convection at the growth surface.

In the transmission topograph shown in Fig. 11 we may notice that the volume defects have in fact the form of thin long pipes. We can notice that they are grouped

into a number of fan-shaped beams, running in different directions. It is difficult to absolutely exclude the existence of dislocations between the pipe-shaped volume defects. It is rather unlikely, however, as no contrasts in the double-crystal topographs resemble the rosettes characteristic for the dislocations outcrops.

In Fig. 12 we report double-crystal and transmission topographs of the neighboring samples, corresponding to same intersection of the crystal parallel to the growth axis. Here the two samples, a thinner one and a thicker, were cut out one close to the other [56]. The thin sample was used for the Lang transmission topography, while the other 1.5 mm thick for the double-crystal topography. The double-crystal topograph shows significant strains connected with the core. After cutting out the samples these strains expanded causing the misorientation of the two parts of the sample located on both sides of the core, which made one half of the sample stay out of reflection. We may notice in the topographs shown in Fig. 12 that the pipe-shaped volume defects appeared also in the middle part of the crystal. It seems to be highly probable that the formation of the volume defects is connected with a strong perturbation of the growth conditions, appearing as growth bands with high contrast. The volume defects appear to start a little bit earlier, but it is in consistence with the interpretation as solute trails. At the moment of perturbation, there was probably constitutional supercooling which triggered local solving of the material inside the already grown crystal. This perturbation is propagated during the next stages of growth of the crystal in a form of a pipe, where the melt crystallize a little later. The other large defect appearing in the middle part of the sample shown in Fig. 13 seems to be an irregularly bounded area of the facetted growth.

The important information concerning the observed volume defects received from the Berg-Barrett topograph shown in Fig. 13 was that the defects can be divided in two categories. In the case of the first one, as in the case of facets in the core, only the extinction contrast at boundaries of the defects becomes visible. It means that the volume of defects reflects X-rays like the rest of crystal. It may be concluded that the first category of the volume defects, similarly to the core contains $Y_3Al_5O_{12}$, probably differing with the concentration of dopant. The second category refers to the defects appearing in the Berg-Barrett topographs as more clear areas; here on the direct copies with black contrast. Most probably they do not reflect the radiation, but reflecting of some small intensity cannot be excluded.

The lack of diffraction may be probably explained by the presence of a different crystallographic phase or higher misorientation exceeding 20°. We tried to examine very carefully the first possibility. For that purpose we performed a number of investigations including the powder diffractometry of powdered material from initial parts of the crystals, X-ray microanalysis and micro Laue-method with beam collimated to 0.1 μm. Careful optical microscopic examination did not reveal any inhomogene-
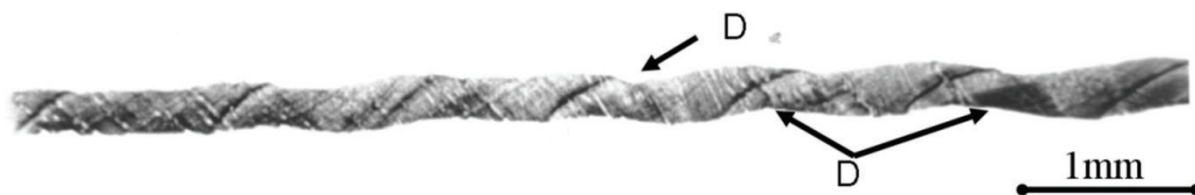
Fig. 14. Synchrotron radiation white beam transmission section topograph for the sample cut from $Ca_{0.5}Sr_{0.5}NdAlO_4$ single crystal, grown by the Czochralski method in $\overline{3}6\overline{7}$ reflection, $\lambda = 0.047$ nm, $\mu t = 2.3$; D denotes characteristic kinks of the section topograph which may indicate the deformation of the crystal lattice – according to A. Malinowska et al. [61].

Rys. 14. Synchrotronowy transmisyjny przekrojowy topogram w wiązce białej próbki wyciętej z monokryształu $Ca_{0.5}Sr_{0.5}NdAlO_4$ otrzymanego metodą Czochralskiego; refleks $\overline{3}6\overline{7}$, $\lambda = 0,047$ nm, $\mu t = 2,3$; D – charakterystyczne stopnie topogramu przekrojowego wskazujące na deformację sieci krystalicznej. Na podstawie A. Malinowska i in. [61].
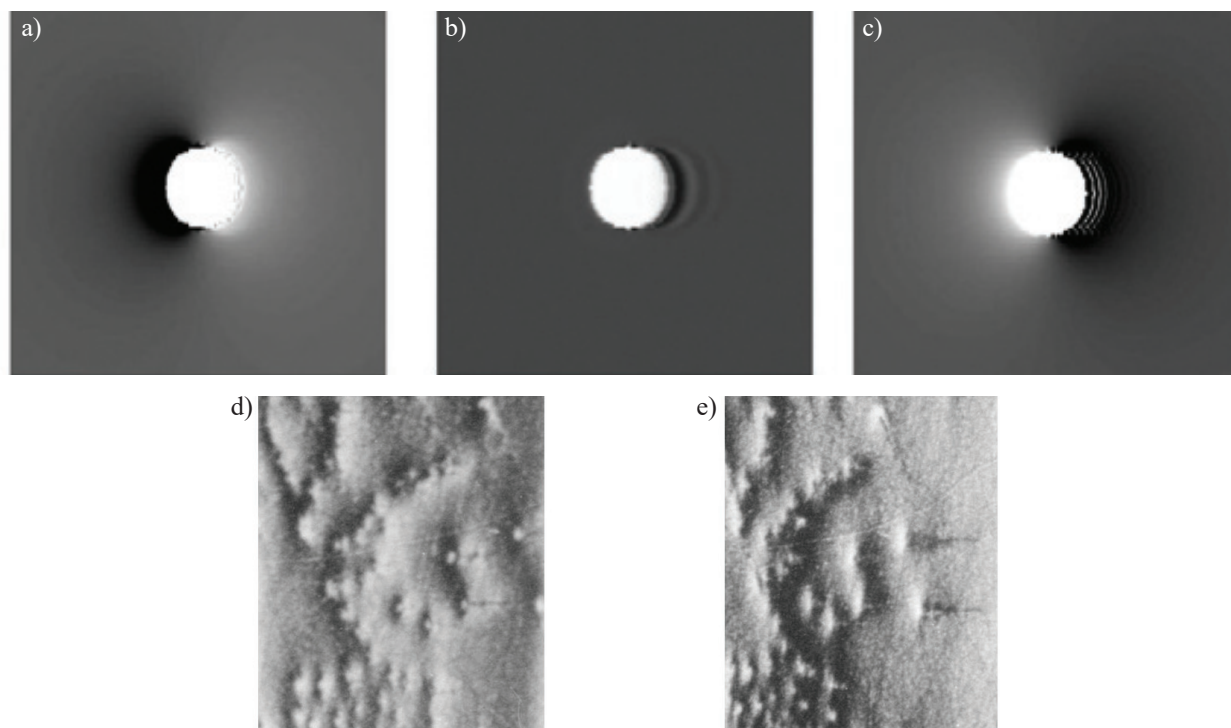

Fig. 15. (a)-(c) Simulated monochromatic beam X-ray topographic images of shrinking rod-like inclusions of 150 μm in diameter for angular setting respectively at low angle flank, maximum and high angle flank of the rocking curve, taken in 008 reflection of 0.1115 nm radiation.(d), (e) monochromatic beam X-ray topographs of volume inclusions in $SrLaGaO_4$ (SLG) crystals exhibiting some features of rod-like inclusions respectively for low and high angle flank of the rocking curve. The contrast of the defects is reversed for the two flanks. According to W. Wierzchowski et al. [57].

Rys. 15. (a) – (c) Symulowane topogramy (dla wiązki monochromatycznej) walcowatego wtrącenia o charakterze ściągającym sieć i średnicy 150 μm; topogram zasymulowany dla trzech różnych ustawień kątowych: na lewym (niskokątowym) zboczu krzywej odbić (a), w maksimum krzywej odbić (b) oraz na prawym (wysokokątowym) zboczu krzywej odbić (c); refleks 008, promieniowanie 0,1115 nm. (d), (e) rentgenowskie dyfrakcyjne topogramy w wiązce monochromatycznej objętościowych wtrąceń w krysztale $SrLaGaO_4$ (SLG) wykazujące cechy walcowych wydzieleni z punktów (a) – (c) odpowiednio dla nisko- i wysokokątowego zbocza krzywej odbić. Widoczne odwrócenie kontrastu dyfrakcyjnego dla obu zboczy krzywej odbić. Na podstawie W. Wierzchowski i in. [57].

ities suggesting the presence of another crystallographic phase. Powder diffractometry did not reveal any peaks apart from those of $Y_3Al_5O_{12}$. It may also be concluded as an important result, because the volume concentration of unreflecting defects evaluated from the ratio of their area to the surface of the sample seem to be greater than 5%, exceeding the sensitivity of the powder diffractometry. X-ray microanalysis did not reveal any detectable change in the concentration of yttrium or aluminium, but an increase of niobium concentration was observed in both

kinds of volume defects and in the core. Both transmission and back-reflection micro-Laue investigation of the nonreflecting volume defects with conventional radiation did not reveal any traces of additional pattern [56].

The synchrotron investigation can reveal significant strains associated with the segregation fringes [61]. In particular they can be revealed in the transmission and reflection section topography. Characteristic results were obtained for $Ca_{0.5}Sr_{0.5}NdAlO_4$ single crystal grown by the Czochralski method in the [100] direction. The crystal
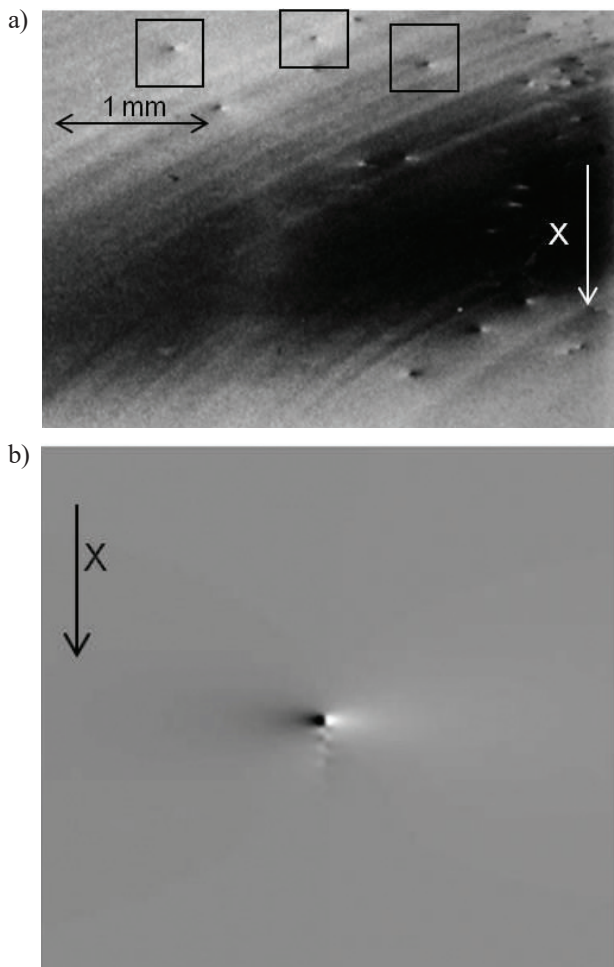
a)

b)

Fig. 16. (a) Monochromatic beam topographic images of dislocation outcrops in the sample cut out from $Y_3Al_5O_{12}$ (YAG); 444 reflection, 0.1115 nm radiation; (b) simulated topographic image of the dislocation outcrop corresponding to the areas limited by squares in (a). According to K. Mazur et al. [70].

Rys. 16. (a) Rentgenowski dyfrakcyjny topogram w wiązce monochromatycznej ujść dyslokacji w próbce wyciętej z monokryształu $Y_3Al_5O_{12}$ (YAG); refleks 444, promieniowanie 0,1115 nm; (b) Symulowany topogram (dla wiązki monochromatycznej) ujścia dyslokacji odpowiadający obszarowi zaznaczonemu przez kwadrat na Rys. (a).Według K. Mazur i in. [70].

seems to be very interesting in the view of its very high lattice parameter changes and strains connected with the composition changes and the presence of large amount of volume defects interpreted as the solute trails. The representative section topograph is shown in Fig.14 [61].

The identification of the solute trails in garnets and $SrLaGaO_4$ (SLG) crystals was confirmed using the simulation based on numerical integration of the Takagi--Taupin equations. The simulation was performed with a model that enabled realistic simulations of the monochromatic beam topographic images of some solute trails in garnets and the Bragg-case section images of some defects resembling rod-like inclusions described in [73]. The approximation of the strain field of rod–like dislocations was obtained by a summation of the contributions

from the point-like inclusions used the formulae derived from those given by Sen [77].

The example of the simulations confirming the expected presence of rod like inclusions in the case of SLG crystals is presented in Fig. 15. The simulation corresponds to an assumed shrinkage type inclusion at the angular setting for low angle flank maximum and a large angle flank respectively.

As the reference in Fig. 16 we quote the experimental and numerically simulated images of dislocations outcrops in YAG substrates according to [70].

Representative synchrotron and conventional topographs of the samples cut out from $(Ca_{0.28}Ba_{0.72})_y(Sr_{0.61}Ba_{0.39})_{1-y}Nb_2O_6$ (CSBN) crystals are shown in Figs. 17 - 18. Contrary to $Sr_xBa_{1-x}Nb_2O_6$ (SBN) and $Ca_xBa_{1-x}Nb_2O_6$ (CBN) crystals we did not observe any glide bands in the CSBN [74]. The most characteristic defects were segregation fringes (marked by S and G) and dislocations or some rod-like inclusions (marked by D) around the core present in the central part of the samples.

The topographs revealed a very characteristic phenomenon, which consisted in the presence of two different sys-
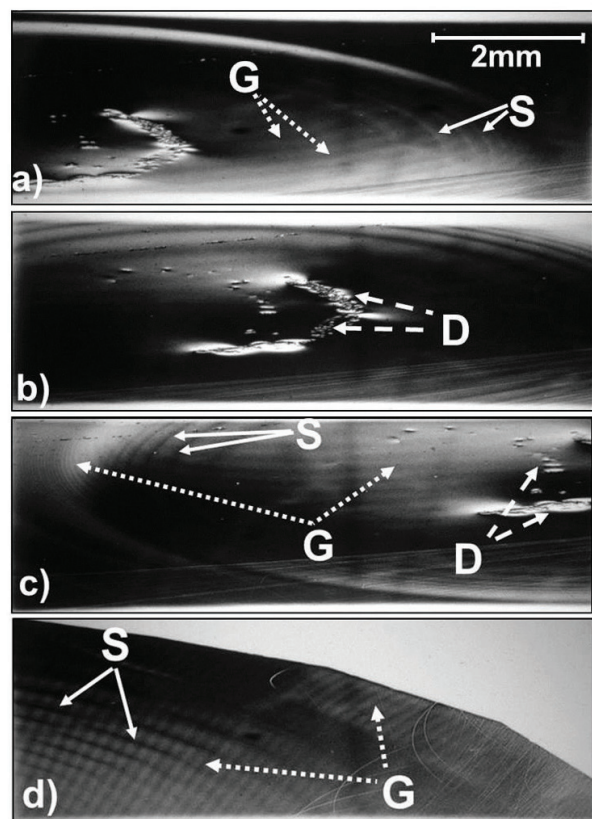

Fig. 17. (a) - (d) Synchrotron monochromatic beam topographs $(Ca_{0.28}Ba_{0.72})_y(Sr_{0.61}Ba_{0.39})_{1-y}Nb_2O_6$ (CSBN) in 004 reflection of 0.1115 nm radiation. According to W. Wierzchowski et al. [74].

Rys. 17. (a) - (d) Synchrotronowe topogramy rentgenowskie w wiązce monochromatycznej monokryształu $(Ca_{0.28}Ba_{0.72})_y(Sr_{0.61}Ba_{0.39})_{1-y}Nb_2O_6$ (CSBN); refleks 004, promieniowanie 0.1115 nm. Na podstawie W. Wierzchowski i in. [74].
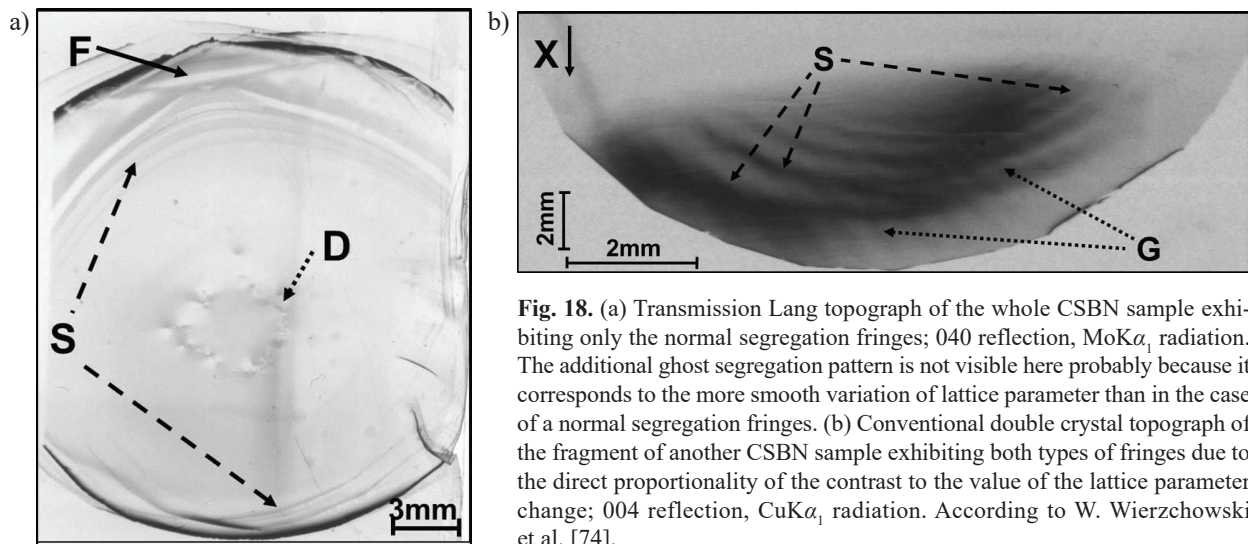
Fig. 18. (a) Transmission Lang topograph of the whole CSBN sample exhibiting only the normal segregation fringes; 040 reflection, MoKα_1 radiation. The additional ghost segregation pattern is not visible here probably because it corresponds to the more smooth variation of lattice parameter than in the case of a normal segregation fringes. (b) Conventional double crystal topograph of the fragment of another CSBN sample exhibiting both types of fringes due to the direct proportionality of the contrast to the value of the lattice parameter change; 004 reflection, CuKα_1 radiation. According to W. Wierzchowski et al. [74].

Rys. 18. (a) Transmisyjny topogram Langa całej próbki wyciętej z monokryształu CSBN ujawniający jedynie zwykłe prążki segregacyjne; refleks 040, promieniowanie MoKα_1. Brak widocznych *ghost segregation pattern* spowodowane jest łagodniejszymi wahaniami parametru sieciowego niż w przypadku zwykłych prążków segregacyjnych; (b) Konwencjonalny topogram dwukrystaliczny fragmentu innej próbki CSBN ujawniający oba rodzaje prążków segregacyjnych dzięki silniejszej zależności kontrastu od nawet małych zmian parametru sieciowego; refleks 004, promieniowanie CuKα_1. Według W. Wierzchowski i in. [74].
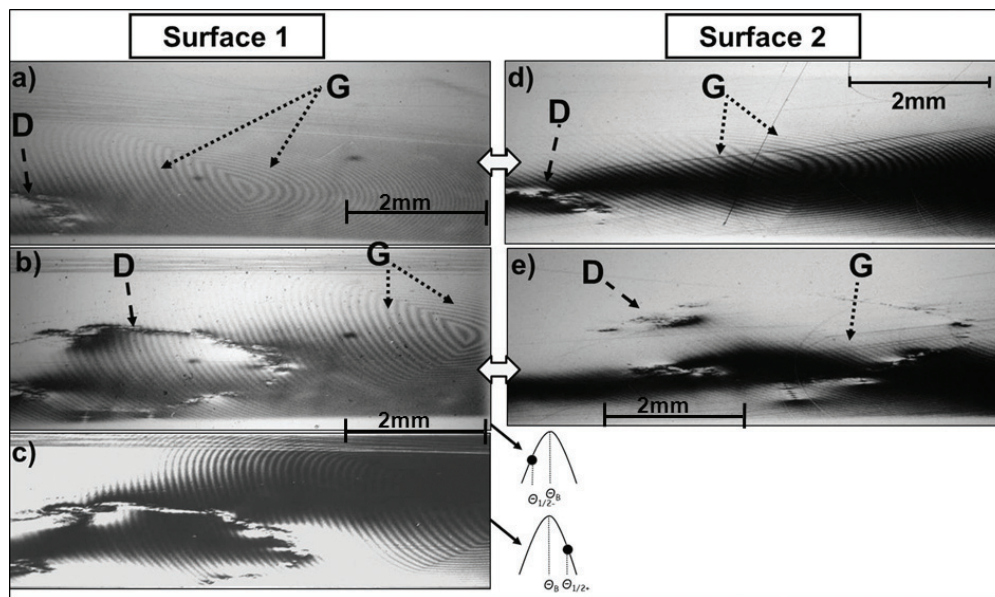

Fig. 19. Synchrotron monochromatic beam back-reflection projection topographs for two surfaces of the (001)-oriented sample cut out from the near-end part of the $(Ca_{0.28}Ba_{0.72})_{0.75}(Sr_{0.61}Ba_{0.39})_{0.25}Nb_2O_6$ (CSBN-75) crystal: (a) - (c) - front surface and (d), (e) - rear surface respectively; (a) shows a characteristic three sector pattern of *ghost* fringes seen also on the other side of the crystal (d); (b), (c) were taken from the middle region of the sample for two flanks of the rocking curve showing the inversion of the contrast of the *ghost* pattern fringes. The middle region of the sample on the other surface is shown in (e); 002 reflection, 0.1115 nm radiation. The width at half maximum of the rocking curve was close to 8.5 arc sec., S - *normal* segregation fringes, G - *ghost* segregation pattern, D - diffraction contrasts corresponding to the defects in the core region. According to W. Wierzchowski et al. [74].

Rys. 19. Synchrotronowe rentgenowskie odbiciowe topogramy projekcyjne w wiązce monochromatycznej dla dwóch powierzchni próbki o orientacji (001) wyciętej z końcowej części monokryształu $(Ca_{0.28}Ba_{0.72})_{0.75}(Sr_{0.61}Ba_{0.39})_{0.25}Nb_2O_6$ (CSBN-75). (a) - (c) - przednia powierzchnia (d), (e) - odpowiednio tylna powierzchnia (a) pokazuje charakterystyczny trójsektorowy układ prążków *ghost fringes*, widoczny również na przeciwnej stronie próbki. (d); topogramy (b), (c) naświetlone w środkowym obszarze próbki dla dwu przeciwnych zboczy krzywej odbicia wykazują odwrócenie się kontrastu prążków *ghost*. Środkowy obszar przeciwnej powierzchni próbki pokazano na topogramie (e); Wszystkie topogramy naświetlano w refleksie 002, dla promieniowania 0,1115 nm. Szerokość połówkowa maksimum krzywej odbicia wynosiła około 8,5 sekund kątowych, Przez S - oznaczono normalne prążki segregacyjne, natomiast przez G - prążki segregacyjne *ghost*, D - oznacza kontrast pochodzący od defektów w obszarze rdzenia. Według W. Wierzchowski i in. [74].

tems of segregation fringes forming a crossing pattern [74]. One of the systems (marked by *S* in Figs. 17 - 18) is connected with the subsequent position of the growth surface being coaxial with the core and the boundaries of the crystal. The second system the so called *ghost* segregation pattern, marked by *G* in Figs. 17 - 19, crossing the previous one, cannot be connected with the position of the growth surface. In addition, investigation of the relatively thick crystal wafers (Fig. 19) confirmed that this fringe system is changing relatively slowly; hence it can propagate through large distances along the growth axis.

The inversion of the diffraction contrast in the monochromatic beam synchrotron topographs from white to black for opposite flanks of the rocking curve (Figs. 19b, c) indicates that the observed contrast of segregation fringes is caused by the slight crystal lattice parameters fluctuations.

Neither scanning electron microscopic investigations nor X-ray microanalysis (with the accuracy 0.5 - 1.0 at. %) revealed any fluctuations of composition corresponding to the systems of segregation fringes.

The possible explanation of the observed phenomenon is a kind of *ghost* segregation pattern reproducing some chemical composition changes in the new part of the growing crystal [74]. The other possibility is connected with the formation of a kind of relief on the growth surface, which was connected with former segregation effects and remained after the change of the growth surface. It is worth to notice that the *ghost* segregation fringes were effectively revealed only by means of the synchrotron monochromatic beam topography and conventional double crystal topography, but were not visible in the transmission Lang topography. This may results from the contrast formation mechanism in the first two methods, where the contrast depends only on the relative lattice parameter changes on the level of 10^{-6}. Contrary to that the Lang topography reveals the segregation fringes thanks to the lattice parameters gradients, which may not be large enough in the *ghost* segregation fringes, where one can expect a significant smoothening in course of propagation of the effect along the crystal. The Lang topograph shown in Fig. 18 reproduced the near-edge part of the crystal containing some faceted growth region (marked by F) similar to the one discussed in [66].

5. Conclusions

Conventional methods of X-ray diffraction topography have been successfully used in many papers describing the growth and the defect structure in oxide crystals grown with various methods especially with the Czochralski method. The possibility of X-ray diffraction topography was significantly increased by the use of synchrotron radiation offering a better resolution and collimation of the beam as well as the possibility of using more suitable radiation

wavelengths. For this reason the synchrotron radiation topography has also been widely used for the investigation of the defect structure of many crystals particularly the oxide crystals.

In the present paper the possibilities of the conventional and synchrotron diffraction topography have been illustrated on the basis of the results obtained by the authors. The paper includes the investigation of the recently developed crystals as well as examples quoted from the previous publications illustrating the studies of the defects characteristic for the oxide crystals in particular the examples of studies of segregation fringes, mosaic structures and solute trails shown together with some applications of the numerical simulations of the defect structure based on the numerical integration of the Takagi-Taupin equations. We also included topographs illustrating the new phenomenon of the simultaneous existence of the two types of segregation fringes called by us the ghost segregation pattern most probably caused by the transmission of some chemical composition changes in the growing crystal.

References

[1] Solski I. M., Sugar Yu D., Vakiv M. M.: Growing Large Size Complex Oxide Single Crystals by Czochralski Technique for Electronic Devices, *Acta Phys. Pol. A*, 2013, 124, 314 – 320

[2] Bruni F. J., Johnston G. M.: Careful system design speeds laser-crystal growth, *Solid State Laser Materials Laser Focus World*, 1994, 205 – 212

[3] Cockayne B., Gates M. P.: Growth striations in vertically pulled oxide and fluoride single crystals, *J. Mat. Science*, 1967, 2, 118 – 123

[4] Carruthers J. R.: Origins of convective temperature oscillations in crystal growth melts, *J. Cryst. Growth*, 1976, 32, 13 – 26

[5] Dąbkowska H. A., Gaulin B. D.: Growth of single crystals of selected cup rates by the optical floating zone technique, *Journal of Optical Electronics and Advanced Materials*, 2007, 9, 1215 – 1220

[6] Dąbkowska H. A., Dabkowski A. B.: Crystal Growth of Oxides by optical Floating Zone, in Springer Handbook of Crystal Growth, Springer, 2010

[7] Brown C. S., Kell R. C., Thomas L. A., Wooster N., Wooster W. A.: The growth and properties of

large crystals of synthetic quartz, *Mineralogical Magazine*, 1952, 29, 858 – 874

[8] Brown C. S., Thomas L. A.: The effect of impurities on the growth of synthetic quartz, *J. Phys. Chem. Sol.*, 1980, 13, 337 – 343

[9] Li W. - J., Shi E. - W., Zhong W. - Z., Yin Z. - W.: Growth mechanism and growth habit of oxide crystals, *J. Cryst. Growth*, 1999, 203, 86 – 196

[10] Zhang S., Yao S., Li J., Zhao L., Wang J., Boughton R. I.: Growth habit control of ZnO single crystals in molten hydrous alkali solutions, *J. Cryst. Growth*, 2011, 336, 56 – 59

[11] McLaren A. C., Cook R. F., Hyde S. T., Tobin R. C.: The mechanisms of the formation and growth of water bubbles and associated dislocation loops in synthetic quartz, *Phys. Chem. Minerals*, 1983, 9, 79 – 94

[12] Tanner B. K.: X-ray diffraction Topography, Pergamon Press, Oxford, 1976

[13] Bowen D. K., Tanner B. K.: High resolution X-ray diffractometry and topography, Taylor and Francis, London, 1998

[14] Authier A.: Dynamical theory of X-ray diffraction, Oxford University Press, Oxford, 2001

[15] Lang A. R.: A method for the examination of crystal sections using penetrating characteristic radiation, *Acta. Metall.*, 1957, 5, 358 – 364.

[16] Lang A. R.: Direct observation of Individual Dislocation by X-Ray Diffraction, *J. Appl. Phys.*, 1958, 29, 597 – 598

[17] Bonse U., Kappler E.,: Röntgenographisches Abbildung des Verzerrungsfeldes einzelner Versetzungen in Germanium-Einkristallen, *Z. Naturforsch.*, 1958, 214, 348 – 349

[18] Bond W. L., Andrus J.: Structural Imperfections in Quartz Crystals, *Am. Minneralogist*, 1952, 37, 622 – 632

[19] Bonse U.: Zur röntgenographishen Bestimmung des Types einzelner Versetzungen in Germanium-Einkristallen, *Z. Phys*, 1958, 153, 278 – 296

[20] Renninger M.: The Asymmetric Bragg Reflection and its Application in Double Diffractometry, *Adv. X-ray Analysis*, 1967, 10, 32 – 36

[21] Renninger M., Doppel diffraktometrische Transmissions-Topographie, *Z. Naturforsch. (a)*, 1964, 19, 783 – 787

[22] Schultz L. G.: Method of using a fine-focus X-ray tube for examining the surface of a single crystal, *Trans. AIME*, 1954, 200, 1082 – 1083

[23] Berg W. F.: Übereinröntgenographische Methode zur Untersuchung von Gitterstörungen an Kristallen, *Naturwissenschaften*, 1931, 19, 391 – 396

[24] Barrett C. S.: A new microscopy and its potentialities, *Trans. Metal. Soc*. AIME, 1945, 161, 15 – 64

[25] Tuomi T., Naukkarinen K., Rabe P.: Use of Synchrotron X-Ray Diffraction Topography, *Phys. Stat. Sol. (a)*, 1974, 25, 93 – 106

[26] Hart M.: Synchrotron radiation - its application to high-speed, high-resolution X-ray diffraction topography, *J. Appl. Cryst.*, 1975, 8, 436 – 444

[27] Tanner B. K., Safa M., Midgley D., Bordas J.: Observation of magnetic domain wall movements by X-ray topography using synchrotron radiation, *J. of Magnetism and Magnetic Materials*, 1976, 1, 337 – 341

[28] Tanner B. K.: Crystal assessment by X-ray topography using synchrotron radiation, *Progress in Crystal Growth and Characterization,* 1976, 1, 23 – 56

[29] Hart M., Sauvage M., Siddons D. P.: White beam synchrotron X-ray interferometry, *Acta Cryst. A*, 1980, 36, 947 – 951

[30] Wheatmore R. W., Goddard P. A., Tanner B. K.: Direct imaging of travelling Rayleigh waves by stroboscopic X-ray topography, *Nature*, 1982, 299, 44 – 46

[31] High-throughput, High-resolution X-ray topography imaging system: XRT micron, *The Rigaku Journal,* 2014, 30, 1

[32] Omote K.: Crystal defects in SiC wafers and a new X-ray topography system, *The Rigaku Journal*, 2013, 29, 1–8

[33] Lang A. R., Miuscov V.F.: Dislocation configurations in magnesium oxide observed by x-ray topography, *Phil. Mag.*, 1964, 10, 263 – 268

[34] Basterfield J., Prescott M. J., Cockayne B.: An X-ray diffraction topographic study of single crystals of melt-grown yttrium aluminium garnet, *J. Material Sci.*, 1968, 3, 33 – 40

[35] Cockayne B., Chesswas M., Born P. J., Filby J. D.: The morphology and defect characteristics of vertically pulled $MgAl_2O_4$ single crystals, *J. Material Sci.*, 1969, 4, 236 – 241

[36] Mag C. A., Shah J. S.: Dislocation reactions and cavitation studies in melt-grown sapphire, *J. Mater. Sci.*, 1969, 4, 179 – 187

[37] Belouet C.:About the crystalline perfection of Nd-doped YAG single crystals, J. Cryst. Growth, 1972, 15, 188 – 194

[38] Neuroth G., Wallrafen F.: Czochralski growth and characterization of pure and doped $YAlO_3$ single crystals, *J. Cryst. Growth,* 1999, 435 – 439

[39] Stacy W. T., Enz U.: The characterization of magnetic bubble-domain materials with X-ray topography, *Trans IEEE Magnetics Mag.*, 1972, 8, 268 – 272

[40] Stacy W. T.: Dislocations, facet regions and growth striations in garnet substrates and layers, *J. Cryst. Growth*, 1974, 24/25, 137 – 143

[41] Spencer W. J., Haruta K.: Defects in Synthetic Quartz, *J. Appl. Phys.*, 1966, 37, 549 – 554

[42] McLaren A. C., Osborne C. F., Saunders L. A.: X-ray topographic study of dislocations in synthetic quartz, *Phys. Stat. Sol. (a)*, 1971, 4, 235 – 247

[43] Takagi M., Mineo H., Sato M.: Defects in synthetic quartz, *J. Cryst. Growth*, 1974, 24/25, 541 – 543

[44] Croxall D. F., Ward R. C. C., Wallace C. A., Kell

R. C.: Hydrothermal growth and investigation of Li-doped zinc oxide crystals of high purity and perfection, *J. Cryst. Growth*, 1974, 22, 117 – 124

[45] Baruchel J., Di Michiel M., Lafford T., Lhuissier P., Meyssonier J., Nguyen-Thi H., Philip A., Pernot P., Salvo L., Scheel M.: Synchrotron X-ray imaging for crystal growth studies, *C. R. Physique*, 2013, 14 (1-2), 208 – 220

[46] Kasper E., Burle N., Escoubas S., Werner J., Oeheme M., Lyutovich K.: Strain relaxation of metastable SiGe/Si: Investigation with two complementary X-Ray Techniques, *J. Appl. Phys.*, 2012, 111, 063507-1 – 063507-10.

[47] Yao S., Hu X., Yan T., Liu H., Wang J., Qin X., Chen Y.: Twinning structures in near-stoichiometric lithium niobate single crystals, *J. Appl. Cryst.*, 2010, 43, 276 – 279

[48] Muehlberg M., Burianek M., Joschko B., Klimm D., Danilewsky A., Gelissen M., Bayarjargal L., Görler G. P., Hildmann B. O.: Phase equilibria, crystal growth and characterization of the novel ferroelectric tungsten bronzes $Ca_xBa_{1-x}Nb_2O_6$ (CBN) and $Ca_xSr_yBa_{1-x-y}Nb_2O_6$ (CSBN), *J. Cryst.Growth*, 2008, 310, 2288 – 2294

[49] Prokhorov I. A., Zakharov B. G., Senchekov A. S., Egorov A. V., Camel D., Tison P.: Structural features of Ge(Ga) single crystals grown by the floating zone method in microgravity, *J. Cryst. Growth*, 2008, 310 (22), 4701 – 4707

[50] Yoneda Y., Mizuki J., Takeda H., Shiosaki T.: X-ray topography of piezoelectric $La_3Ta_{14}Ga_{5.5}O_{14}$ crystal grown by Czochralski Method, *IEEE Trans. Ultrason. Ferroelectr. Freq. Control*, 2008, 55 (5), 971 – 974

[51] Yao G.D., Hou S.Y., Dudley M., Phillips J.M.: Synchrotron X-ray Topography Studies of Twin Configurations in Lanthanum Aluminate Single Crystals, *J. Mater. Res.*, 1992, 7, 1847 – 1855

[52] Dudley M., Yao G. D.: Synchrotron Topography of Phase Transitions in Perovskite-Like Crystals, *J. Phys. D*, 1993, 26, A120 – A125

[53] Cerva H., Graeff W.: Contrast investigations of surface acoustic waves by stroboscopic topography II Wave field deviation contrast, *Phys. Stat. Sol. (a)*, 1985, 87, 507 – 516

[54] Wieteska K.: X-ray topography using synchrotron radiation, *Acta Physica Polonica A*, 1994, 86, 545 – 552

[55] Malinowska A., Lefeld-Sosnowska M., Härtwig J.: Contrast in transmission X-ray diffraction topographs of growth defects in the core of $SrLaGaO_4$ single crystals, *J. Appl. Cryst.*, 2013, 46, 48 – 54

[56] Mazur K., Wierzchowski W.: X-ray topographic investigation of growth defects and lattice parameter measurements within crystals of heavily neodymium doped yttrium aluminium garnet, *J. Cryst. Growth*, 1995, 148, 345 – 354

[57] Wierzchowski W., Wieteska K., Malinowska A., Wierzbicka E., Lefeld-Sosnowska M., Świrkowicz M., Łukasiewicz T., Pajączkowska A., Paulmann C.: Synchrotron Diffraction Topography in Studying of the Defect Structure in Crystals Grown by the Czochralski Method, *Acta Phys. Pol. A*, 2013, 124, 350 – 356

[58] Wieteska K., Wierzchowski W., Wierzbicka E., Malinowska A., Lefeld-Sosnowska M., Łukasiewicz T., Graeff W.: X-ray topographic studies of defects structure in YVO_4 crystal, *Acta Phys. Pol. A*, 2008, 114 (2), 455 – 461

[59] Wierzbicka E., Malinowska A., Wieteska K., Wierzchowski W., Lefeld-Sosnowska M., Świrkowicz M., Łukasiewicz T., Paulamann C.: Characterization of the Defect Structure in Gadolinum Orthovanadate Single Crystals Grown by the Czochralski Method, *Acta Phys. Pol. A*, 2012, 121, 906 – 909

[60] Wieteska K., Wierzchowski W., Graeff W., Lefeld-Sosnowska M., Pajączkowska A., Wierzbicka E., Malinowska A.: Investigation of the defect distribution along the growth direction in GdCOB crystals by synchrotron and conventional X-ray topography, *J. Aloys. Comp.*, 2005, 401, 69 – 74

[61] Malinowska A., Lefeld-Sosnowska M., Wieteska K., Wierzchowski W., Graeff W., Pajaczkowska A.: X-ray topography of $Ca_{0.5}Sr_{0.5}NdAlO_4$ single crystal, *J. Cryst. Growth*, 2008, 310 (14), 3398 – 3402

[62] Lefeld-Sosnowska M., Olszyńska E., Wierzchowski W., Wieteska K., Graeff W., Pajączkowska A., Kłos A.: Conventional and synchrotron radiation back reflection topography of $GdCa_4O(BO_3)_3$ crystals, *J. Alloys. Comp.*, 2004, 382, 153 – 159

[63] Wieteska K., Wierzchowski W., Malinowska A., Turczyński S., Lefeld-Sosnowska M., Pawlak D.A., Łukasiewicz T., Paulmann C.: Synchrotron Topographic Studies of Domain Structure in Czochralski Grown $Pr_xLa_{1-x}AlO_3$ and $Pr_xLa_{1-x-y}Mg_yAlO_3$ Crystals, *Acta Phys. Pol. A*, 2012, 121, 910 – 914

[64] Wieteska K., Wierzchowski W., Malinowska A., Turczyński S., Lefeld-Sosnowska M., Pawlak D. A., Łukasiewicz T., Graeff W.: X-ray Topographic Investigations of Domain Structure in Czochralski Grown $Pr_xLa_{1-x}AlO_3$ Crystals, *Acta Phys. Pol. A*, 2010, 117, 268 – 271

[65] Wieteska K., Wierzchowski W., Malinowska A., Lefeld-Sosnowska M., Świrkowicz M., Łukasiewicz T., Paulmann C.: Synchrotron diffraction topography of $Sr_xBa_{1-x}Nb_2O_6$ (SBN), $Ca_xBa_{1-x}Nb_2O_6$ (CBN) and mixed $(Ca_{0.28}Ba_{0.72})_y(Sr_{0.61}Ba_{0.39})_{1-y}Nb_2O_6$ (CSBN) crystals, *Rad. Phys. Chem.*, 2013, 93, 87 – 91.

[66] Kołodziejak K., Wierzchowski W., Wieteska K., Malinowski M., Graeff W., Łukasiewicz T.: The Investigation of structural perfection and faceting in highly Er-doped $Yb_3Al_5O_{12}$ Crystals, *Cryst. Res. Technol.*, 2008, 43, 369 – 373

[67] Wierzchowski W., Wieteska K., Graeff W., Sakowska H., Łukasiewicz T., Pawłowska M.: Synchrotron X-ray investigation of $La_{0.3}Sr_{0.7}Al_{0.65}Ta_{0.35}O_3$ crystals, *Cryst. Res. Technol.* 2005, 40, 517 – 522

[68] Savytskii D., Senyshyn A., Matkowskii A., Vaylech-

ko L., Wieteska K., Wierzchowski W., Łukasiewicz T., Bismayer U.: White beam synchrotron X-ray topography studies of twinning in GdFeO$_3$-type perovskite crystals, *Z. Kristallogr.*, 2003, 218, 17 – 25

[69] Malinowska A., Lefeld-Sosnowska M., Wieteska K., Wierzchowski W., Härtwig J., Graeff W.: Synchrotron topographic studies of growth defects in the core of a SrLaGaO$_4$ crystals, *Phys. Stat. Sol. (a)*, 2009, 206, 1816 – 1819

[70] Mazur K., Sarnecki J., Wierzchowski W., Wieteska K., Turos A.: X-ray characterization of GGG homoepitaxial layers with introduced divalent Ni ions, *Rad. Phys. Chem.*, 2011, 80, 1084 – 1087

[71] Mazur K., Sarnecki J., Borysiuk J., Wierzchowski W., Wieteska K., Turos A.: X-ray study of gadolinium gallium garnet epitaxial layers containing divalent Co ions, *Thin Solid Films*, 2011, 519, 2111 – 2115

[72] Paszkowicz W., Romanowski P., Bąk-Misiuk J., Wierzchowski W., Wieteska K., Graeff W., Iwanowski R.J., Heionnen M.H., Ermakova O., Dąbkowska H.A.: Characterization of an Yb:LuVO$_4$ single crystal using X-ray topography, high-resolution X-ray diffraction, and X-ray photoelectron spectroscopy, *Rad .Phys. Chem.*, 2011, 80, 1001 – 1007

[73] Balcer T., Wierzchowski W., Wieteska K.: The Simulation of Bragg-Case Section Images of Dislocations and Inclusions in Aspect of Identification of Defects in SiC Crystals, *Acta Phys. Pol. A*, 2010, 117, 336 – 340

[74] Wierzchowski W., Wieteska K., Malinowska A., Wierzbicka E., Romaniec M., Lefeld-Sosnowska M., Świrkowicz M., Łukasiewicz T., Sakowska H., Paulmann C.: *Ghost* segregation pattern and ferroelectric domains in mixed calcium-strontium barium niobates, *X-ray Spectrometry*, 2015, 44, 356 – 362

[75] Wierzbicka E., Malinowska A., Wieteska K., Wierzchowski W., Lefeld-Sosnowska M., Świrkowicz M.,

Łukasiewicz T., Paulmann C.: Characterization of crystal lattice defects in calcium molybdate single crystals (CaMoO$_4$) by means of X-ray diffraction topography, X-ray Spectrometry, 2015, 44, 351 – 355

[76] Authier A.: Contrast of dislocation images in X-ray transmission topography, *Advan. X-ray Analysis*, 1967, 10, 9 – 31

[77] Sen B.: Note on the stresses produced by nuclei of thermo-elastic strain in a semi-infinite elastic solid, *J. Quant. Mech*, 1949, VIII (4), 365 – 369

[78] http://www.esrf.eu/home/UsersAndScience/Experiments/StructMaterials/ID19/Techniques/Diffraction/Overview.html (online 2018)

[79] Wierzbicka E., Malinowska A., Wierzchowski W., Kisielewski J., Świrkowicz M., Szyrski W., Romaniec M., Mazur K.: Rentgenowska topografia dyfrakcyjna defektów sieci krystalicznej w monokryształach MgAl$_2$O$_4$ i ScAlMgO$_4$ otrzymywanych w różnych warunkach technologicznych, *Materiały Elektroniczne (Electronic Materials)*, 2015, 43, 1, 29 – 39

[80] Malinowska A., Wierzbicka E., Wierzchowski W., Mazur K., Romaniec M., Kisielewski J., Świrkowicz M., Szyrski W., Drozdowski W.: Badanie struktury defektowej w nowych rodzajach scyntylacyjnych monokryształów mieszanych granatów lutetowo--itrowo-glinowych [Lu$_x$Y$_{1-x}$]$_3$Al$_5$O$_{12}$ (LuYAG) niedomieszkowanych oraz aktywowanych prazeodymem, *Materiały Elektroniczne (Electronic Materials)*, 2015, 43, 1, 11 – 28

[81] Świrkowicz M., Szyrski W., Kisielewski J., Wieteska K., Wierzchowski W., Malinowska A., Wierzbicka E., Karaś A., Jurkiewicz-Wegner E.: Wzrost monokryształów molibdenianu wapnia domieszkowanych jonami ziem rzadkich (CaMoO$_4$:RE) do badań w zakresie immobilizacji odpadów radioaktywnych, *Materiały Elektroniczne (Electronic Materials)*, 2013, 41, 4, 10 – 19

LIST OF REVIEWERS 2016